Graduate University of Advanced Technology

Journal of Geological Remote Sensing

Journal homepage: https:// jgrs.kgut.ac.ir

Iranian Geological Remote Sensing Society

Mapping of rock outcrops as a prerequisite for lithogeochemical sampling surveys based on the spatial distribution analysis: an application of ASTER data, southern Iran

Samira Shayganpour[1], Majid Hashemi Tangestani[1*]

[1] *Department of Earth Sciences, Faculty of Sciences, Shiraz University, 71454 Shiraz, Iran*

Article Info

Keywords:
Sub-pixel mapping
metamorphic rock
soil-adjusted vegetation index
mixture-tuned match filtering
maximum likelihood
Kowli-kosh metamorphic complex

Abstract

Rock outcrops are generally covered by vegetation and the Quaternary deposits, so their enhancement on the satellite imagery can be impeded, and the identification of pixels of rock outcrops be a challenging task for field sampling in lithogeochemical surveys. Therefore, in order to map outcrops of different rock types, it is required, first, to estimate the distribution of vegetation and the Quaternary deposits as the major step for field sampling in lithogeochemical surveys. This paper is an attempt to map outcrops of different rock types as a prerequisite for lithogeochemical sampling surveys in Kowli-kosh metamorphic complex in Sanandaj-Sirjan zone (SSZ). To evaluate the efficacy of this approach, geochemical anomalies of Cu, Au, and Fe in samples collected from enhanced rock outcrops of a metamorphosed area were analyzed. In order to obtain the objectives of study, we firstly utilized the maximum likelihood (ML), soil-adjusted vegetation index (SAVI), and mixture-tuned matched filtering (MTMF) methods on reflective bands of advanced space-borne thermal emission and reflection radiometer (ASTER) to map the Quaternary deposits, vegetation, and lithological units in Kowli-Kosh metamorphic complex, SW Iran. Pixels matched to lithological units were identified wherever the matched filter (MF) scores were > 0.65. These areas were then cross-tabulated with vegetation and Quaternary maps to differentiate the representative areas of rock outcrops. A grid network was subsequently generated and overlaid on the map of rock outcrops, and the rock chip samples for lithogeochemical analysis were collected from cells containing more than 15 pixels of rock outcrops. The spatial distribution analysis of rock types and the geochemical statistics showed that there is a strong relationship between outcrops and the anomalies of the desired elements. It was concluded that the approach introduced by this study improved the potentials usage of ASTER data in mapping of the areas covered by vegetation and Quaternary deposits. This approach help inobtaining a perspective on conducting lithogeochemical sampling surveys in order to manage cost-effective exploration operations in such areas.

*Corresponding author.
Email: *tangestani@susc.ac.ir*
https://doi.org/10.48306/jgrs.2023.364670.1000
Received 6 October 2022; Received in revised form 25 January 2023; Accepted 29 May 2023
Available online August 2023

1. Introduction

An overview on the land surface of the Earth shows that outcrops of rocks do not form the major parts of it, basically due to the coverage of vegetation and the Quaternary sediments (Howell, 1960). In point of geological view, the outcrops of rock units allow the geologists to observe them directly, and to sample the bedrocks in situ, aiming the various disciplines such as geological studies, lithogeochemical analysis, and compiling the geological maps.

On the other hand, lithogeochemical studies fundamentally seek to find out the chemical composition of bedrocks/rocks that are appeared at the ground surface (Dunlop et al., 1979). This primary dispersion of geochemical compositions in bedrock can guide the geologists to explore the probable exploration targets (James, 1967). Lithogeochemical surveys are generally performed through a network or during field traverses, with samples collected from accessible rock outcrops. Selection of specific rock types for sampling could ideally be implemented after a lithological map is available (Govett and Ian, 1979). Therefore, recognizing the spatial pattern of rock outcrops as well as their lithologies is crucial for conducting lithogeochemical sampling surveys. In this regard, utilizing the satellite imagery in mapping areas that show the highest match to lithological units, and these are without vegetation and soil cover, is a remarkable endeavor.

When dealing with any geological field sampling surveys based on the processing of satellite data, it is evident that the Earth surface is mostly composed of mixed materials, among which, in landscape scales, the Quaternary deposits and vegetation are more common. These materials can directly affect recognizing the pixels of rock outcrops (Fraser and Green, 1987; Carranza and Hale, 2002; van der Meer et al., 2012). Meanwhile, although the forest with large canopies does not grow in arid and semi-arid climates, the growth of shrubs and rangeland can play an important role in preventing the enhancement of underneath rocks. Furthermore, Quaternary deposits that originate from upstream rocks would modify the spectral responses of pixels, and consequently, may affect the accuracy of enhanced pixels due to different spectral characteristics of these deposits.

For decades, remote sensing geologists have produced lithology and mineral maps by the use of satellite data (e.g., Abdelsalam and Stern., 2000; Azizi et al., 2010; Ibrahim et al., 2018; Zimmermann et al., 2016; Rogge et al., 2014; Noori et al., 2019; Bolouki et al., 2020); however, displaying pixels of rock outcrops has been a fundamental problem so far. Kang et al. (2017) applied Landsat-8 images for accurate identifying and mapping exposed rock outcrops in Antarctica. Drake et al. (1999) successfully mapped geological features, soils, and vegetation by the use of spectral matching on AVIRIS SWIR data. Enhancement of lithologies in a vegetated district using the TM data of Landsat was implemented by Crippen and Blom (2001). They suggested that a significantly strong lithologic signal will remain after the vegetation signal is suppressed. Grebby et al. (2014), used Airborne Thematic Mapper (ATM) data to study the impact of vegetation on mapping rock types in Troodos ophiolite, Cyprus, and concluded that useful lithological information could be obtained by the using appropriate data

processing methods, despite the dense vegetation and limited spectral sampling.

Meanwhile, the Advanced Space-borne Thermal Emission and Reflection Radiometer (ASTER) imagery (Fujisada, 1995; Abrams, 2000) with 20 years' history of applications in lithology and alteration mapping, is still the unique freely available satellite data with global coverage and applicable spectral bands for geologists (Abdeen et al., 2001; Rajendran et al., 2011, 2016 and 2018; Testa et al., 2018). The improvements in spectral and spatial resolutions of this instrument encouraged the remote sensing geologists to apply them extensively for mineral exploration in arid to semi-arid regions. It measures three spectral bands in the VNIR region between 0.52 and 0.86 μm with 15-m spatial resolution, which are applicable for mapping the vegetation and Fe-oxides in rocks and soils. This sensor also measures the radiation of the short wave infrared (SWIR) region in six bands between 1.65 and 2.40 μm with pixel size of 30 m. This region of spectrum is well-known for its capability in mineralogical and lithological mapping. The thermal infrared (TIR) radiation is also measured in five spectral bands between 8.12 and 11.65 μm by ASTER, which geologically are useful for detecting silica contents of rock units. These capabilities have already been used for exploration of different ore deposits and mapping of various rock types (Calvin et al., 2015; Rezaei et al., 2020; Khalifa et al., 2020; Ishagh et al., 2021; Manap and San., 2022).

Moreover, it is approved that the multispectral data of ASTER can be very useful for delineating the interesting areas on the ground that need more detailed attention during the subsequent field works. For instance, Salem et al. (2016) presented new gold prospecting areas in the alteration zones at Dungash district, southeastern Egypt, by ASTER data. They applied output results of data processing as well as field observation and petrographic-geochemical studies to distinguish alterations as probable targets for Au exploration. Testa et al., (2018) highlighted rock type outcrops in the Frontal Cordillera, western Argentina by the use of a logical operation on the ASTER data. Amer et al., (2016) proved successful utilization of ASTER imagery for enhancements of sericite, calcite, and clay minerals in the Central Eastern Desert of Egypt.

Review of the previously published articles shows that despite the various geological applications of ASTER data, there are lack of research on dealing with enhancement of vegetation- and soil-free rock outcrops in the literature. The rock outcrops without vegetation and Quaternary colluvial and alluvial deposits can be representative locations of lithogeochemical sampling, because they allow identification of the spatial pattern of specific rock types (Kruse et al., 2003) that can support identifying the exploration targets before field observation and sampling. Such investigations can lead to optimizing field works and sampling numbers in areas covered by vegetation and Quaternary deposits.

This study was an attempt to map rock outcrops with no vegetation- and soil coverage in order to be used as a guideline for lithogeochemical sampling surveys, aiming at exploration of Au, Cu, and Fe. Soil-adjusted vegetation index (SAVI), maximum likelihood (ML) method, and mixture tuned matched filtering (MTMF) algorithm were applied to map vegetation, Quaternary sediments, and highly matched pixels to the spectral characteristics of rock

types, respectively. The vegetation- and soil-free areas were then extracted through a spatial distribution analysis in the GIS environment, and the lithogeochemical sampling survey was conducted on them. Subsequently, the spatial relationships between rock type outcrops and the geochemical analysis results of collected samples were investigated. The case study is Kowli-Kosh metamorphic complex, south of Iran (Fig. 1), which consists of various schistose rocks with anomalous concentrations of Au, Cu, and Fe (Jafarian, 2009; Shahidi, 2010).

2. Geology and mineralization

The study area is part of the Kowli-kosh metamorphic complex in Sanandaj-Sirjan zone (SSZ), 200 km north of Shiraz, southern Iran (Fig. 1). This complex is illustrated in the geological maps of Dehbid and Eqlid, published at a scale of 1:100,000 (Geological Survey of Iran 2009a, b). Regional structures at the area show a general trend of NW-SE (Alavi, 1994), and the dominant lithologies include chlorite-epidote schist, mica schist, meta-diorite, meta-tuff, meta-andesite, meta-limestone, and rhyolite (Jafarian, 2009; Shahidi, 2010). Of interest to mineral exploration, this area hosts several occurrences of metallic sulfides and oxides, some of which contain economic quantities of Au, Cu, and Fe (Houshmandzadeh, 1990). The most important lithologic units which contain these anomalies are chlorite-epidote schist, mica schist, and volcanic rocks (Jafarian, 2009; Shahidi, 2010). In general, all rocks that have undergone regional deformation and metamorphism can be suitable host rocks for gold deposits (Rahmani, 2008; Jafarian, 2009; Shahidi, 2010); however, a strong positive correlation has already been reported between green schist and meta-diorite with gold content (Rahmani, 2008).

Evidences of two copper-gold indices are observed at Zooli Valley (Fig. 1), western part of the study area, known as Basiran-1 and Basiran-2 (Rahmani, 2008). The dominant lithologies associated with these indices include metamorphosed mafic rocks, mica schist, and chlorite schist in Basiran-1, and meta-diorite, chlorite schist, and meta-limestone in Basiran-2 (Rahmani, 2008). Native gold, realgar, and scheelite are reported as indicators of Au mineralization at the area. The Cu mineralization is also approved by occurrences of chalcopyrite, chalcocite, pyrite, and malachite (Fig. 9) (Rahmani, 2008; Jafarian, 2009; Shahidi, 2010). Iron mineralization is extensive by the presence of magnetite and hematite, associated with Fe-hydroxides such as goethite and jarosite (Rahmani, 2008).

Kowli-Kosh area is located in a high-altitude semi-arid climate covered by pasture and shrub (Fig. 2) as well as small cultivated lands and gardens. Based on the geological maps, the Quaternary deposits commonly include recent clastic deposits with variable textures, which are the eroded sediments of upstream rock units (Fig. 1c). These sediments, as well as vegetation, partly obscure the rock units.

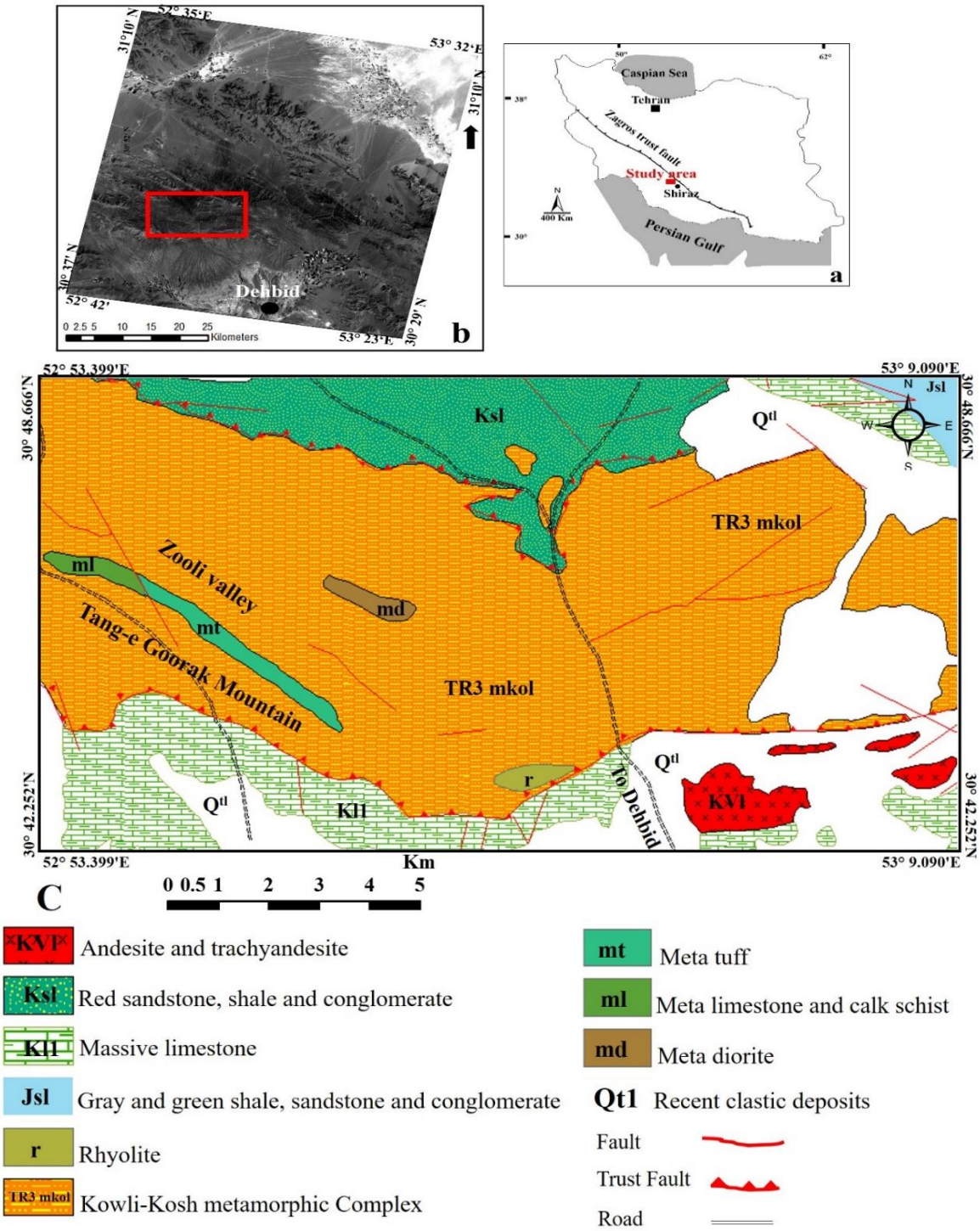

Fig. 1. a) geographic position of the study area in Iran; b) position of the Kowli-kosh complex in ASTER image in red rectangle; and c) geological map of the study area (modified from 1: 100,000 geological maps of Eqlid and Dehbid)

.

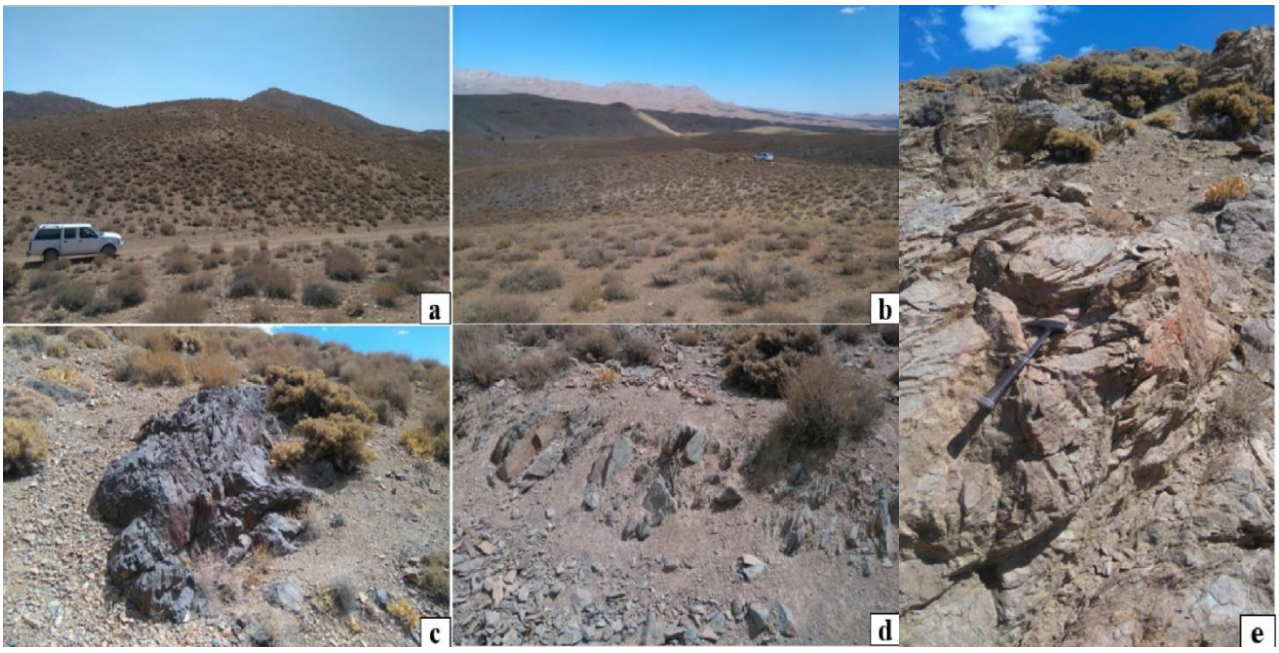

Fig. 2. Field photographs showing mixture of vegetation and Quaternary sediments covering a) mica schist; b) chlorite-epidote schist and meta-diorite; c) meta-andesite; d) chlorite-epidote schist; and e) meta-limestone

.

3. Data and methods

The ASTER data applied in this study were acquired in August 2001, in the level 1T. The VNIR and SWIR datasets of a region of interest with 827 × 1672 pixels (Fig. 1b) were stacked to obtain a 9-bands data set with pixel sizes resampled to 15×15 m.

In order to obtain the distribution map of vegetation- and sediment-free outcrops of rock types, it was first required to map the Quaternary deposits, vegetation, and lithology. These outcrops were subsequently applied for facilitating the field sampling surveys aiming lithogeochemical investigations. In this research, we proposed a method for facilitating the field sampling surveys aiming for lithogeochemical analysis. The geochemical concentrations of Cu, Au, and Fe in the collected samples were measured and were spatially compared with extracted outcrops of rock types. To obtain the objectives of this research, the following steps were pursued: 1) converting the raw data to reflectance by the use of Log Residuals technique (Green and Craig, 1985; Conel et al., 1987) and geometric correction of imagery by the use of topographic maps in scale of 1:25000; 2) applying the maximum likelihood (Isermann, 1988; Richards, 1999) and SAVI (Huete, 1988) methods for mapping the Quaternary deposits and vegetation density; 3) spectral characterization of rock types collected in the field, and extraction of end-members' spectra from calibrated imagery; 4) sub-pixel mapping and classification of lithological units using a mixture tuned matched filtering (MTMF) algorithm (Boardman, 1998); 5) extracting the vegetation- and sediment-free outcrops of rock types through a cross-tabulation procedure in GIS environment (Pontius, 2000 and 2002; Congalton and Green, 1999); 6) planning field survey and sampling of rock outcrops

in a proposed grid network for lithogeochemical analysis; 7) geochemical analysis of collected samples and estimating the anomalies of Au, Cu, and Fe; and 8) to investigate the relationships between each rock type and the anomalies of Cu, Au, and Fe; 9) assessing the accuracy of results by the use of a combination of confusion matrix, Kappa coefficient, stuy of microscopic thin sections, and field observations. More important methods are described below in details.

3.1. Maximum Likelihood

Maximum likelihood (ML) classifier (Isermann, 1988) determines the likelihood that a given pixel of an imagery belongs to a particular class, supposing that the distribution statistics for each class in each band are Gaussian. Considering the results of this method, each pixel is allocated to the class that shows the highest likelihood (Richards, 1999). Equation [1] reveals how the maximum likelihood classifier calculates the probabilities for each pixel of the imagery:

[1]
$$g_i(x) = \ln p(\omega_i) - {}^1/_2 \ln |\Sigma_i| - {}^1/_2 (x - m_i)^T \Sigma_i^{-1} (x - m_i)$$

where: *i is* the *i*th class, *p(ωi)* is the same likelihood for occurrence of a class in the image, *x is n*-dimensional data in which n defines the number of bands, |Σi| is determinant of the covariance matrix of the data in a class, m_i is mean vector of a class, and Σi^{-1} is inverse of the covariance matrix of a class. This algorithm has frequently been used by geologists (e.g. Ivanov and Poltavchenko, 1988; Wester, 1991).

In the present study, we conducted this algorithm on the ASTER data, during which, two classes including alluvial and colluvial deposits were introduced as training areas to the algorithm. Each deposit type was defined in a total of 380 pixels according to geological map (Fig. 1). The selected pixels were randomly subdivided into 2/3 training, and 1/3 testing pixels. The mapping results were assessed by investigating their distribution in geological maps and through the field observations.

3.2. Soil-Adjusted Vegetation Index

The soil-adjusted vegetation index (SAVI) method (Huete, 1988) was used to map the vegetation densities. Based on the logic of this method, vegetation index values can be influenced by the reflectance of red and near-infrared light, where the area is covered by a combination of low vegetation (i.e., < 40%) and the soil. When applying SAVI [Eq. 2] in areas possessing dense vegetation, parameter L is 0; whereas in barren lands, L=1. However, in most geographical conditions, L=0.5 works well (Johnson, 1998) and is the default value, which is also applied in the present study.

$$\text{SAVI} = \frac{b_3 - b_2}{b_3 + b_2 + L} \times (1+\text{L}) \qquad [2]$$

In this equation, b3 and b2 are reflectances in calibrated bands 3 and 2 of ASTER. The output results of SAVI method were divided into 4 classes based on the density of vegetation.

3.3. Mixture tuned matched filtering

The general concept of Mixture Tuned Matched Filtering (MTMF) algorithm is based on partial unmixing of pixels in the imageries through

estimation of the degree of match of a given pixel to a reference spectrum (Boardman, 1998). This method can also approximate the sub-pixel abundances of end-members, which, in fact, are the surface features that their spectra are introduced to the algorithm. Matched filtering (MF) score in the MTMF algorithm shows a degree of match between the target spectra and the spectra of pixels in the original image, so that score of one is a perfect match. The MTMF algorithm is frequently applied by geologists (e.g. Rowan and Mars, 2003; Zhang et al., 2007; Tayebi et al., 2015).

The spectra of chlorite-epidote schist, mica schist, meta-limestone, meta-diorite, and meta-andesite were extracted from the ASTER imageries. These were then compared with the corresponding spectra extracted from the spectral libraries and the spectra of collected rock samples, measured at the Central Laboratory of NIRS (Near-infrared spectroscopy) instrument which is active in the Central Laboratory of Shiraz University, Shiraz, Iran, to ascertain their spectral characteristics. The approved image spectra of rock types were introduced to the algorithm as references, and the degree of match of lithologies with the reference spectra was assessed. Although the MTMF algorithm is capable of estimating the sub-pixel quantity of the target materials, in this study, we interpreted the results of this technique for recognizing the highest correspondences of lithological units only.

3.4. Spatial distribution analysis and field sampling

Combination of two maps obtains a new map that can be quantitatively studied for finding the correspondence between them with summary statistics based on the subsets defined by spatial or thematic information (Bonham-Carter, 1994). Pontius (2004) evaluated the total change of land classes by the use of cross-tabulation matrix. Shalaby and Tateishi (2007) applied a cross-tabulation procedure for post-classification change detection on outputs of Landsat in the Northwestern coast of Egypt. Also, Henriques et al. (2015) applied cross-tabulation to investigate the role of lithology on the pattern of landslides.

In order to achieve the spatial relationships of vegetation, Quaternary deposits, and lithology maps, they were first converted to the vector format. These vector maps were then spatially integrated by the use of overlay operation in a GIS environment. The spatial distribution interpretation of these vector maps was conducted through a cross-tabulation procedure to find the vegetation- and sediment-free outcrops of various rock types.

Subsequently, a 1 × 1 km grid network was generated for the study area and was overlaid on the map of rock outcrops (Fig. 8). Field sampling for lithogeochemical analysis of Cu, Au, and Fe was then conducted on those grid cells which contained more than 15 pixels of rock outcrops**.** In cases that more than one lithological unit outcropped in a 1 × 1 km grid cell, sampling was carried out on both outcrops and altered areas, probable mineralized zones, and wherever the silicate veins were observed. Thus, 118 chip samples were collected and were geochemically analyzed in Zarazma Company, Tehran, Iran, by ICP-OES and Fire assay methods.

4. Results and discussion

4.1. Mapping Quaternary deposits and vegetation

Classes of Quaternary deposits were mapped by the use of maximum likelihood classification method and the accuracy of outputs was evaluated by the confusion matrix and Kappa statistics. The testing areas for Quaternary deposit types were selected randomly based on the geological map and the Google Earth imagery. The overall accuracy and Kappa coefficient were estimated 93.18% and 0.87, respectively. Moreover, the visual comparison of processed imagery to the geology map of the study area represented a favorable conformity. However, considering the scale of geology map (1:100,000) comparing to the pixel size of the applied imagery, more detailed and extensive areas were enhanced through the image processing. Finally, the output classes were dissolved and a homogenous information layer (Fig. 3), namely "Quaternary deposits", was generated.

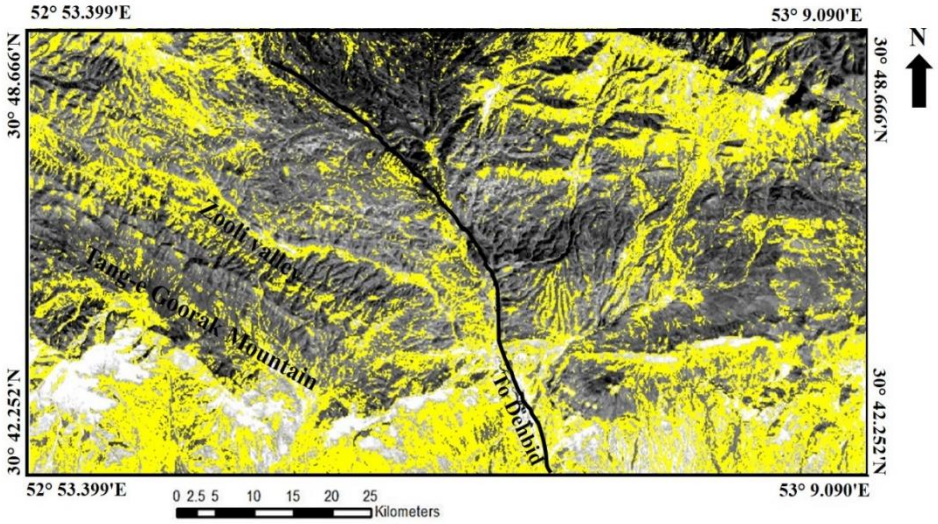

Fig. 3. Quaternary deposit map produced by combination of output classes of maximum likelihood algorithm

The SAVI algorithm mapped vegetation density of the area in a range of -0.4 to +0.4 which was qualitatively reclassified into "very low", "low", "moderate", and "high" densities (Fig. 4). The reclassified map showed dominant vegetation densities for low and moderate classes (57.34% and 29.44%, respectively). It was also observed that pixels with high density of vegetation corresponded with the gardens and a combination of grasses and trees grown in stream lines.

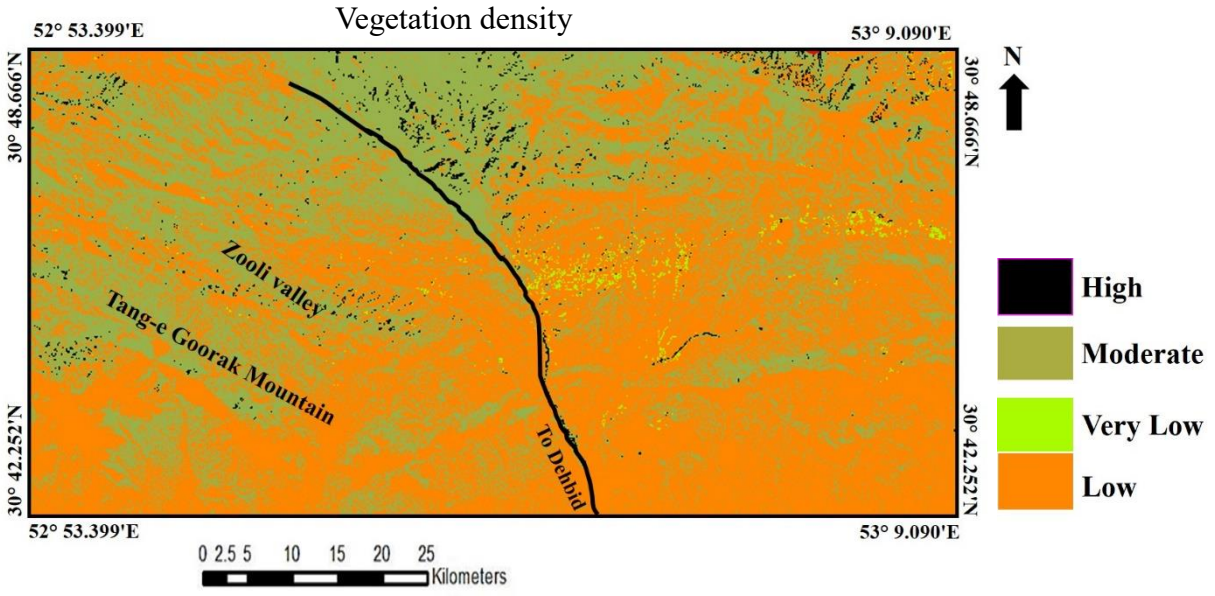

Fig. 4. Vegetation density classification, produced by SAVI method; the density classes are presented in the legend.

4.2. Mapping lithological units

The resampled spectra of meta-andesite, meta-diorite, chlorite-epidote schist, mica schist, and meta-limestone to the ASTER bands, as well as ASTER-derived spectra of similar rock types, are shown in Figure 5. The spectra of meta-diorite display strong absorption bands near 0.69 µm and 0.87µm due to the iron electronic processes (Clark 1990; Hunt 2017) and near 2.34µm for Fe-Mg-OH vibrations (Clark et al. 1993; Gupta 2017); which correspond with bands 2, 3, and 8 of ASTER (Fig. 5a). Meta-andesite shows an absorption feature near 0.5 µm that could be attributed to iron electronic processes (Clark 1990; Hunt 2017), and near 2.1 µm, 2.25 µm, and 2.34 µm due to vibrational modes of Al-OH, Mg-OH and Fe-OH, respectively (Clark et al. 1993; Gupta 2017). Chlorite-epidote schist displays spectral absorption features near 2.25 µm and 2.34 µm, due to vibrational modes of Fe-OH and Mg-OH (Clark et al. 1993; Gupta 2017). The image spectra of this rock type show major absorption features in bands 2 and 8 of ASTER (Fig. 5-c). Reflectance spectra of mica schist shows an absorption feature near 0.5 µm due to iron electronic processes (Clark 1990; Hunt 2017) and near 2.21µm, attributed to hydroxyl and Al-OH. The major absorption features of this rock type are shown in bands 2 and 6 of the ASTER (Fig. 5-d). The diagnostic absorption feature of meta-limestone is near 2.31µm (band 8 in Fig. 5-e) because of the vibrational mode of CO_3 (Clark 1990; Hunt 2017). The ASTER-derived spectra of dominant rock types were input as end-member references to the MTMF algorithm and their degree of match to the applied bands was mapped accordingly.

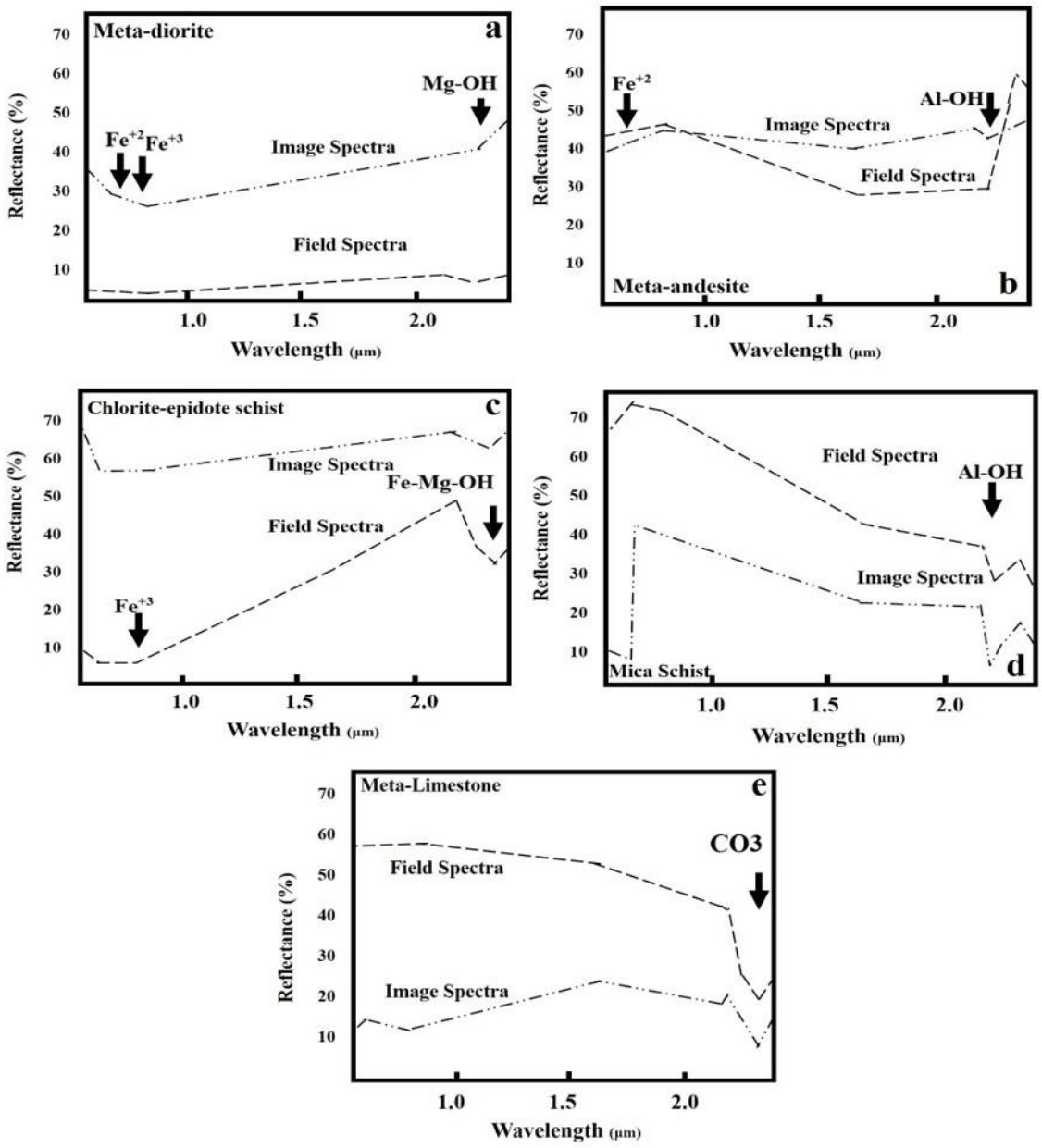

Fig. 5: The spectra of rock types extracted from the VNIR-SWIR bands of ASTER as well as their

measured spectra, resampled to similar bands; important absorption features are shown with arrows.

The matched filter scores of rock units were produced and pixels with scores of > 0.65 for each rock type were selected to show the spatial distribution of the desired lithology. These pixels were then demonstrated in different colors on a gray scale image (Fig. 6). The discriminated rock types coincided well with their relevant outcrops at 1:100.000 geological maps and the evidences collected in the field and microscopic studies of thin

sections. However, limited mapped outcrops in figure 6, comparing to the geology map (Fig. 1c), is due to the fact that these pixels only represent the matched filter scores > 0.65 for the relevant rock types.

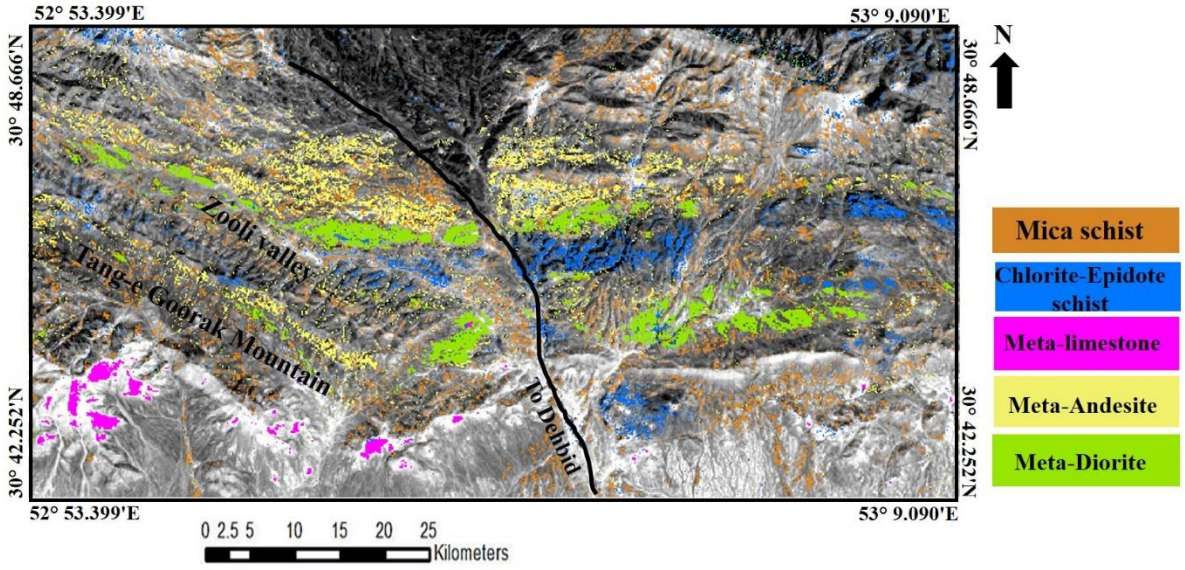

Fig. 6. Fraction maps for matched filter scores more than 0.65 of mica schist, meta-diorite, chlorite-epidote schist, meta-limestone, and meta-andesite, demonstrated on a gray image of ASTER.

4.3. Spatial distribution analysis of lithology, vegetation, and Quaternary deposits

The vegetation- and soil-free outcrops of rock units (Fig. 7) were extracted using spatial distribution analysis of vegetation, Quaternary deposits, and lithology maps through a cross-tabulation procedure in GIS. The study area dominantly consists of Quaternary deposits (60.56%; 129 km^2) which are partly covered by rangelands with low and moderate densities. The maximum cross coverage of lithologies is occurring in low-vegetation districts (29.52% of total area), which means that pixels of lithologies are typically enhanced in areas that the density of vegetation is low. Furthermore, the cross coverage of lithologies with high-vegetation areas is only 4.46%, which means that only 0.58% of lithology pixels are covered by high-density rangeland. On the other hand, results of MTMF revealed that the highest distribution of lithologies belong to chlorite-epidote schist (10.33 km^2), while the minimum spatial distribution belongs to meta-limestone, covering 1.31 km^2 of the study area.

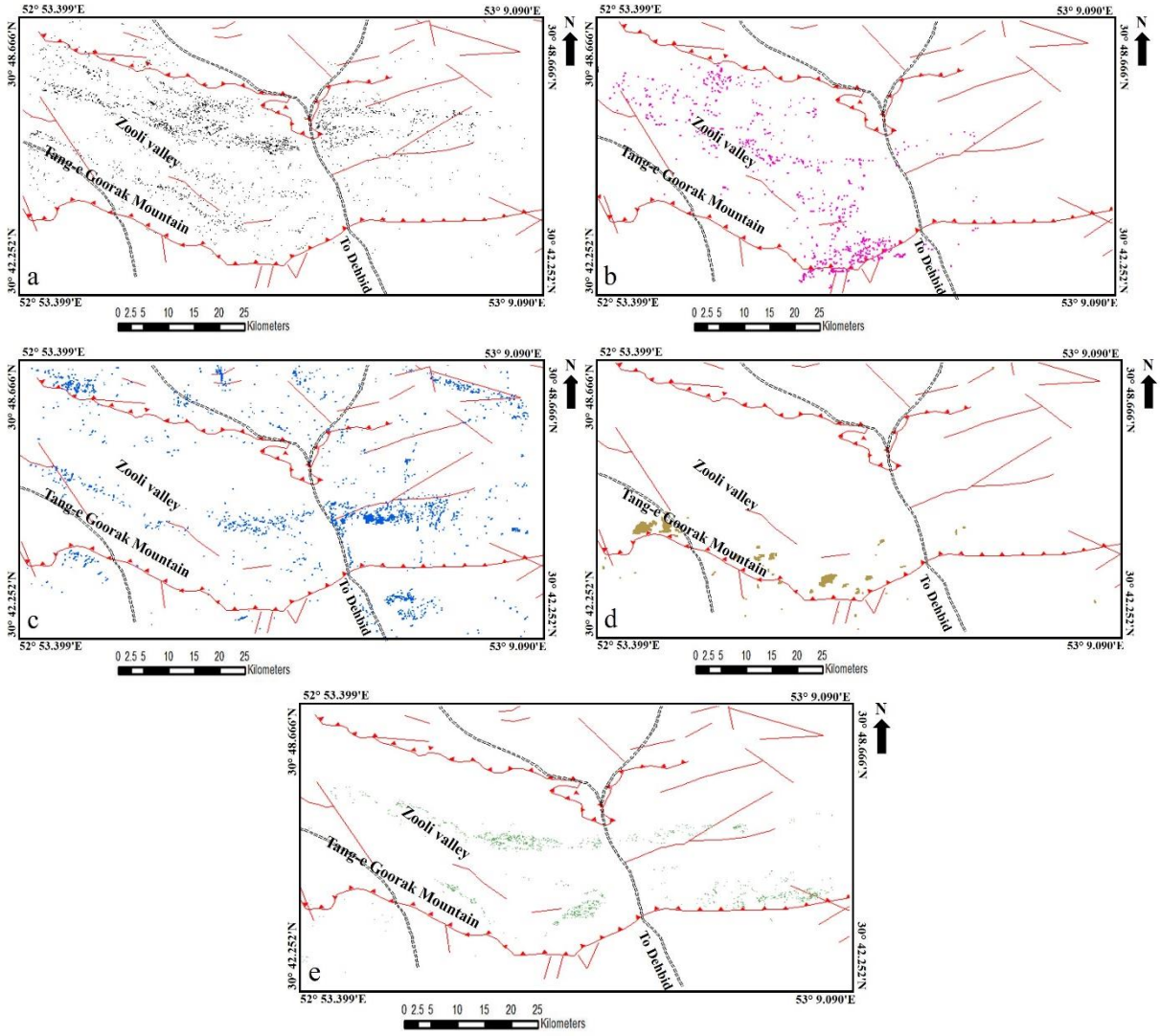

Fig. 7: Spatial distribution of vegetation- and soil-free outcrops of: a) chlorite-epidote schist, b) mica schist, c) meta-andesite, d) meta-limestone, and e) meta-diorite.

4.4. Relationships between rock type outcrops and geochemical anomalies

The objective of this part of the study was to investigate the lithogeochemical anomalies for Fe, Cu, and Au, and identifying their relationships with vegetation- and soil-free outcrops of different rock types.

The study area was gridded, with one square kilometer cell size in ArcGIS and rock samples were collected from outcrops that were extracted in the previous step. This survey was conducted on those cells that contained more than 15 pixels of rock outcrops (Fig. 8); thus, representative rock samples were collected from 118 cells.

The lowest abundances of Au, Cu, and Fe were 1.1 ppb, 384 ppm, and 20427 ppm, respectively and their highest concentrations were 250 ppb, 2.7%, and 87999 ppm. Analyzing the spatial relationships between rock type outcrops, and the concentrations measured geochemically for the rock samples showed anomalous abundances (but not economically valuable) of Au, Cu, and Fe in 44, 73, and 37 samples, respectively.

Results also showed that Au anomalies are basically occurring in meta-diorite, chlorite-epidote schist, and mica schist, while Cu anomalies are dominantly revealed in meta-diorite. Moreover, Fe was more highly occurring in outcrops of meta-andesite and mica schist. The spatial correlation between rock outcrops and the geochemical anomalies is well distinguished in Cu-Au indications of Basiran-1 and Basiran-2 (Fig. 8) which are occurring in outcrops of chlorite-epidote schist and meta-diorite, respectively.

Field observations in outcrops showed mineralization evidences such as quartzite and malachite veins as well as hematite deposits, and the petrographic investigations approved the occurrence of chlorite, calcite, quartz, and sericite. Furthermore, polished thin sections of similar samples showed opaque and ore minerals, such as pyrite, chalcopyrite, magnetite, and hematite (Fig. 9).

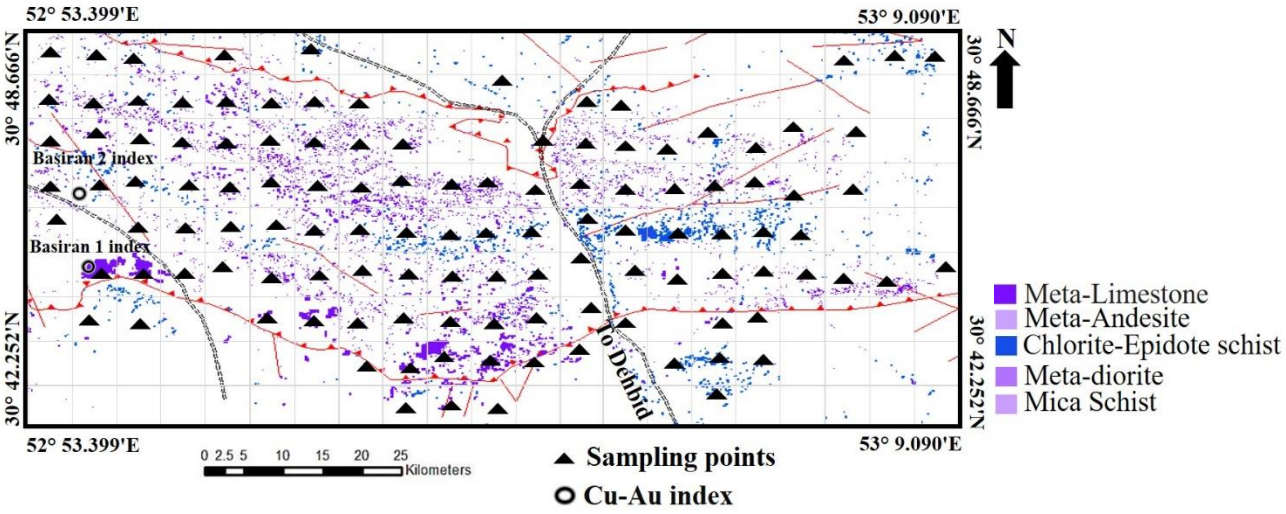

Fig. 8: 1 × 1 km grid network overlaid on the pixels with rocks exposure and the sampled cells for lithogeochemical analysis

Fig. 9. Field observation of a) silica vein and alteration of schist; b) occurrences of chalcopyrite malachite, and magnetite; c) microscopic pictures of Cu and Fe mineralization, Ccp: Chalcopyrite, Hem: Hematite, Py: Pyrite, and Gal: Galena.

5. Summary and conclusions

This study investigated the potential of ASTER data to optimize rock sampling surveys aiming lithogeochemical investigations in areas with limited outcrops of rocks due to vegetation and Quaternary sediment covers. Soil-adjusted vegetation index, maximum likelihood, and mixture tuned matched filtering methods were applied to map vegetation, Quaternary sediments, and lithological units, respectively. MF scores of output pixels in MTMF algorithm were used to identify the degree of match to the spectra of lithologies, thus the values > 0.65 were considered as a desired match for each rock type.

Spatial distribution analysis on vegetation, Quaternary sediment, and lithology maps obtained outcrops of rock types lacking the effective concentrations of vegetation and/or Quaternary deposits. The pixels of outcrops were then used to govern the sampling surveys aiming lithogeochemical prospecting for Au, Cu, and Fe. This, effectively delineated favorable from unfavorable areas in field observations and provided an objective sampling scheme. The sampling sites were chosen from cells of a grid network containing acceptable numbers of pixels of rock outcrops. Geochemical analysis of samples collected from outcrops led to investigating the spatial relationships between the concentrations of Au, Cu, and Fe, and the rock outcrops being sampled. It showed that anomalous concentrations of these elements corresponded to meta-diorite, chlorite-epidote schist, and mica schist.

It is concluded that the approach introduced by the current study leads to a more improved discernment of the mapping potentials of ASTER data in areas where rock units are covered by vegetation and Quaternary deposits. This approach not only helps the geologists to manage their field sampling surveys, but also saves cost and time in lithogeochemical exploration projects and investigating the spatial relationships between rock outcrops and the anomalies of desired elements.

6. References

Abdeen MM, Allison TK, Abdelsalam MG, Stern RJ. Application of ASTER band-ratio images for geological mapping in arid regions; the Neoproterozoic Allaqi Suture, Egypt. Abstract with Program Geological Society of America 2001; 3(3): 289.

Abdelsalam M, Stern R. Mapping gossans in arid regions with Landsat TM and SIR-C images, the Beddaho alteration zone in northern Eritrea. Journal of Africa/Earth Sciences 2000; 30 (4): 903-916.

Abrams B, Stecker M. The Solar System and Beyond.: Structures in Space 2000. doi: 10.1007/978-1-4471-0441-4_1.

Alavi M. Tectonics of the Zagros orogenic belt of Iran: new data and interpretations. Tectonophysics 1994; 229: 211–238.

Amer R, Mezayen AE, Hasanein M. ASTER spectral analysis for alteration minerals associated with gold mineralization. Ore Geology Reviews 2016; 75: 239–251.

Azizi H, Tarverdi MA, Akbarpour A. Extraction of hydrothermal alterations from ASTER SWIR data from east Zanjan, northern Iran. Original Research. Article Advances in Space Research 2010; 46: 99-109.

Bolouki S, Ramazi H, Maghsoudi A, Pour A, Sohrabi G, See fewer. A remote sensing-based application of bayesian networks for epithermal gold

potential mapping in Ahar-Arasbaran area, NW Iran. Remote Sensing 2020; 12(1). doi:10.3390/rs12010105

Boardman JW. Leveraging the high dimensionality of AVIRIS data for improved sub-pixel target unmixing and rejection of false positives: mixture tuned matched filtering. In Summaries of the Seventh Annual JPL Airborne Geoscience Workshop 1998; (6). Pasadena, CA.Bonham-Carter, G.F. Introduction to GIS. Geographic Information Systems for Geoscientists Pages 1994; 1-23. doi:10.1016/b978-0-08-041867-4.50006-0.

Calvin WM, Little field EL, Kratt C. Remote sensing of geothermal-related minerals for resource exploration in Nevada. Geothermics 2015; 53 (1): 517-526.

Carranza EJM, Hale M. Mineral imaging with Landsat Thematic Mapper data for hydrothermal alteration mapping in heavily vegetated terrane. International Journal of Remote Sensing 2002; 23, 4827–4852.

Clark RN, Gallagher AJ, Swayze GA. Material Absorption Band Depth Mapping of Imaging Spectrometer Data Using a Complete Band Shape Least-Squares Fit with Library Reference Spectra, Proceedings of the Second Airborne Visible/Infrared Imaging Spectrometer (AVIRIS) Workshop. JPL Publication 1990; 90-54, 176-186.

Clark RN, Swayze GA, Gallagher A, King TVV, Calvin WM. The U.S. Geological Survey, Digital Spectral Library: Version 1: 0.2 to 3.0 microns: U.S. Geological Survey Open File Report 1993; 1340: 93-592. http://speclab.cr.usgs.gov.

Conel J E. AIS-2 radiometry and a comparison of methods for the recovery of ground reflectance, in Proc. 3rd Airborne Imaging Spectrometer Data Analysis Workshop, G. Vane, Ed, 18–47, Jet Propulsion Laboratory, JPL Publication 1987; 87–30, Pasadena, CA.

Congalton RG, Green K. Assessing the Accuracy of Remotely Sensed Data: Principles and Practices 1999; (New York: Lewis).

Crippen R E, Blom R G. Unveiling the lithology of vegetated terrain in remotely sensed imagery. Photogrammetric Engineering and Remote Sensing 2001; 67, 935-943.

Drake NA, Mackin S, Settle JJ. Mapping vegetation, soils and geology in semi-arid shrublands using spectral matching and mixture modelling of SWIR AIRIS imagery, Remote Sensing Environment 1999; 68, 12-25.

Dunlop R H, Bueno L. Molasses neuro-toxicity and higher volatile fatty acids in sheep. Ann. Rech. Vét 1979; 10 (2-3): 462-464.

Fraser SJ, Green AAA. Software defoliant for geological analysis of band ratios. International Journal of Remote Sensing 1987; 8: 525–532.

Fujisada H. Design and performance of ASTER instrument. Proceedings of SPEI, International Society of Optical Engineering 1995; 2583: 16-25.

Geological Survey of Iran. Geological map of Eqlid, scale 1: 100,000. Geological Survey of Iran 2009a.

Geological Survey of Iran. Geological map of Dehbid, scale 1: 100,000. Geological Survey of Iran 2009b.

Govett GJS, Nichol Ian. Lithogeochemistry in mineral exploration; in Geophysics and Geochemistry in the Search of Metallic Ores; Peter J. Hood, editor; GeolOgical Survey of

Canada, Economic Geology Report 1979; 31: 339-362.

Grebby S, Cunningham D, Tansey K, Naden J. The Impact of Vegetation on Lithological Mapping Using Airborne Multispectral Data: A Case Study for the North Troodos Region, Cyprus. International Journal of Remote Sensing 2014.

Green AA, Craig MD. Analysis of aircraft spectrometer data, with logarithmic residuals, Proceedings of the Airborne Imaging Spectrometer Data Analysis Workshop, April 8-10, G. Vane and A. Goetz editors, JPL 1985; 111-119.

Gupta RP. Imaging Spectroscopy. Book: Remote Sensing Geology 2017; 203-219. doi:10.1007/978-3-662-55876-8_14.

Henriques C, Zêzere J L, Marques F.The role of the lithological setting on the landslide pattern and distribution. Engineering Geology 2015; 189: 17–31.

Houshmandzadeh A. Geological report of Eqlid Sheet (1: 250,000). Geological Survey of Iran 1990; map no. G 10.

Howell J V. Glossary of geology and related sciences. American Geological Institute, Washington 1960; 207-208

Huete AR. A Soil-Adjusted Vegetation Index (SAVI). Remote Sensing of Environment 1988; 25: 295-309.

Hunt G R. Spectroscopic properties of rocks and minerals. In Handbook of Physical Properties of Rocks 2017; (295-386). CRC Press.

Ivanov N V, Poltavchenko V. N. Remote sensing imagery in the study of settlement on alluvial fans. Mapping Sciences and Remote Sensing 1998; 25 (2): 128-134

Ibrahim E, Barnabé P, Ramanaidou E, Pirard E. Mapping mineral chemistry of a lateritic outcrop in New Caledonia through generalized regression using Sentinel-2 and field reflectance spectra. International Journal Applied Earth Observation Geoinformation 2018; 73: 653–665.

Ishagh, M.M, Pour, A.B, Benali, H. *et al.* Lithological and alteration mapping using Landsat 8 and ASTER satellite data in the Reguibat Shield (West African Craton), North of Mauritania: implications for uranium exploration. *Arab J Geosci* 2021; 14: 2576. https://doi.org/10.1007/s12517-021-08846-x

Isermann R. Maximum-Likelihood-Methode. Book: Identifikation dynamischer Systeme. Pages 1988; 1-16. doi:10.1007/978-3-642-97069-6_1.

Jafarian F. Geological report of Eqlid Sheet (1: 100,000). Geological Survey of Iran 2009; map no. G 10.

James CH. The use of the terms "primary" and "secondary" dispersion irl geochemical prospecting; Econ. Geo 1967; 62: 997-999.

Johnson RD. Change vector analysis: a technique for multispectral monitoring of land cover and condition. Remote sensing 1998; 19: 411-426.

Kang J, Cheng X, Hui F, Ci T. An Accurate and Automated Method for Identifying and Mapping Exposed Rock Outcrop in Antarctica Using Landsat 8 Images. IEEE Journal of Selected Topics in Applied Earth Observations and Remote Sensing PP 2017; (99): 1-11. doi:10.1109/JSTARS.2017.2755502.

Kruse F A, Boardman J W, Huntington J F. Evaluation and Validation of EO-1 Hyperion for Mineral Mapping: in Special Issue, Transactions on Geoscience and Remote Sensing (TGARS), IEEE 2003; 41(6): 1388 – 1400.

Noori L, Pour BA, Askari G, Taghipour N, Pradhan B, Lee CW, Honarmand M. Comparison of Different Algorithms to Map Hydrothermal Alteration Zones Using ASTER Remote Sensing Data for Polymetallic Vein-Type Ore Exploration: Toroud–Chahshirin Magmatic Belt (TCMB), North Iran. Remote Sensing 2019; 11: 495; doi:10.3390/rs11050495.

Manap, H.S, San, B.T. Data Integration for Lithological Mapping Using Machine Learning Algorithms. *Earth Sci Inform* 2022; **15**: 1841–1859.

Pontius RG. Quantification error versus location error in comparison of categorical maps. Photogrammetric Engineering and Remote Sensing 2000; 66:1011–1016.

Pontius RG. tatistical methods to partition effects of quantity and location during comparison of categorical maps at multiple resolutions. Photogrammetric Engineering and Remote Sensing 2002; 68:1041–1049.

Pontius RG. Shusas, E. and Mceachern, M. Detecting important categorical land changes while accounting for persistence. Agriculture, Ecosystems and Environment 2004; 101: 251–268.

Rahmani S. Control promising exploration zones based on the Eqlid 1:100,000 sheet. Geological Survey of Iran 2008.

Rajendran S. Mapping of Neoproterozoic source rocks of the Huqf Supergroup in the Sultanate of Oman using remote sensing. Ore Geology Reviews 2016; *78*: 281-299. doi:10.1016/j.oregeorev.2016.03.024.

Rajendran S, Nasir S. ASTER capability in mapping of mineral resources of arid region: A review on mapping of mineral resources of the Sultanate of Oman. Ore Geology Reviews 2018.

Rajendran S, Thirunavukkarasu A, Balamurugan G, Shankar K. Discrimination of iron ore deposits of granulite terrain of Southern Peninsular India using ASTER data. Journal of Asian Earth Sciences 2011; *41*(1), 99-106.

Research Systems Inc. ENVI Tutorial, ENVI Software Package, Version 4.0.

Richards, J.A., and X. Jia., 1999. Remote Sensing Digital Image Analysis, Springer, New York 2003; 225–228.

Robert F, Brommecker R, Bourne B, Dobak PJ, Mcewan C, Rowe RR, ad Zhou X. Models and exploration methods for major gold deposit types. Ore Deposits and Exploration Technology 2007; 48: 691-711.

Rogge D, Rivard B, Segl K, Grant B, and Feng J. Mapping of NiCu–PGE ore hosting ultramafic rocks using airborne and simulated EnMAP hyperspectral imagery, Nunavik, Canada. Remote Sensing of Environment 2014; 152: 302–317.

Rowan LC, Mars JC. Lithologic mapping in the Mountain Pass, California area using advanced spaceborne thermal emission and reflection radiometer (ASTER) data. Remote Sensing of Environ 2003; 84 (3), 350–366.

Rezaei A , Hassani H, Moarefvand P and Golmohammadi A. Geology, Ecology and Landscapes 2020; 4(1): 59-70.

Salem SM, Sharkawi M El, El-Alfy Z, Soliman NM, Ahmed SE. Exploration of gold occurrences in alteration zones at Dungash district, Southeastern Desert of Egypt using ASTER data and geochemical analyses. Journal of African Earth Sciences 2016; 117: 389-400.

Shahidi S. Geological report of Dehbid Sheet (1: 100,000). Geological Survey of Iran 2010; map no. G 10.

Shalaby A, Tateishi R. Remote sensing and GIS for mapping and monitoring land cover and land-use changes in the Northwestern coastal zone of Egypt, Applied Geography 2010; 27(1): 28-41.

Tayebi MH, Tangestani MH, Vincent RK. Sub-pixel mapping of iron-bearing minerals using ALI data and MTMF algorithm, Masahim volcano, SE Iran. Arabian Journal Geosciences 2015; 8 (6): 3799–3810.

Testa F, Villanueva C, Cooke D, Zhang L. Lithological and Hydrothermal Alteration Mapping of Epithermal, Porphyry and Tourmaline Breccia Districts in the Argentine Andes Using ASTER Imagery. Remote Sensing 2018; 10 (203). doi:10.3390/rs10020203.

Van der Meer FD, Van der Werff HMA, van Ruitenbee FJA, Hecker CA, Bakker WH, Noomen MF, van der Meijde M, Carranza EJM, de Smeth JB, Woldai T. Multi- and hyperspectral geologic remote sensing: A review. International Journal of Applied Earth Observation Geoformation 2012; 14: 112–128.

Wester K. User defined classification method for lithological mapping using Landsat TM data. CH2971-0/91/0000-2074$01.OO 01991IEEE 1991; 2074-2078.

Zimmermann R, Brandmeier M, Andreani L, Mhopjeni K, Gloaguen R. Remote Sensing Exploration of Nb-Ta-LREE-Enriched Carbonatite (Epembe/Namibia). Remote Sensing 2016; 8**:** 620-680; doi:10.3390/rs8080620